POAC'13
Espoo, Finland

Proceedings of the 22nd International Conference on
Port and Ocean Engineering under Arctic Conditions
June 9-13, 2013
Espoo, Finland

2D FEM-DEM SIMULATIONS OF PUNCH THROUGH TESTS: EFFECTS OF PARTLY CONSOLIDATED RUBBLE DEFORMATION

Arttu Polojärvi[1,2] and Jukka Tuhkuri[1,2]
[1]Aalto University, School of Engineering, Department of Applied Mechanics
P.O. Box 14300, FI-00076 Aalto, Finland
[2]Sustainable Arctic Marine and Coastal Technology (SAMCoT), Centre for Research-based Innovation (CRI), Norwegian University of Science and Technology, Trondheim, Norway
e-mail: arttu.polojarvi@aalto.fi

ABSTRACT

We modelled punch through tests on partly consolidated ice rubble using 2D combined finite-discrete element method (FEM-DEM). We ran simulations with various freeze bond strengths and block to block friction coefficients. In this paper, we demonstrate the close relation of rubble failure and deformation patterns to indentor load records. We show that the buoyant load component due to the rubble becoming detached from the surrounding rubble field, and displacing during an experiment, is of crucial importance in interpretation of punch through test results in terms of ice rubble material properties.

INTRODUCTION

Punch through experiments are widely used in arctic engineering for testing ice rubble properties. In a punch through experiment, a flat indentor platen penetrates through the floating ice rubble mass while the force applied by the rubble on the indentor is measured. The force records are then used to derive some rubble material properties. Several authors have performed full scale and laboratory scale punch through experiments. These experiments are reviewed in Liferov and Bonnemaire (2005).

A number of authors, e.g. Liferov et al. (2003); Heinonen (2004); Serré (2011), have simulated punch through experiments using continuum models. We demonstrated in Polojärvi et al. (2012) that the continuum description potentially renders out some important phenomena within the rubble. To avoid this, we modelled the rubble as discontinuum using combined finite-discrete element method (FEM-DEM) (Munjiza et al., 1995; Munjiza, 2004). Discontinuum modelling has been earlier used in ice mechanics by e.g. Hopkins (1992) and Paavilainen et al. (2009).

In this paper we concentrate on the effects of rubble deformation patterns on indentor load records in the case of partly consolidated rubble. First, we briefly describe the simulations and then we introduce and discuss the results. The paper only includes a few findings from our punch through test simulations. A comprehensive description of our FEM-DEM model and more results can be found from Polojärvi and Tuhkuri (2013).

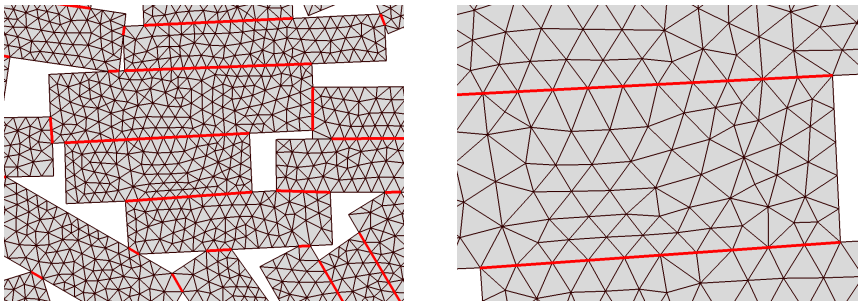

(a) (b)

Figure 1: Snapshots from a simulation showing (a) few ice blocks in a rubble being (b) bonded together by freeze bonds (red).

SIMULATIONS

In our FEM-DEM model, each ice block within the rubble, the contact forces between the blocks, the deformation of the blocks, and the rubble freeze bonds were modelled. For modelling these phenomena, the blocks are meshed into finite elements (see Figure 1a). In addition to contact forces, the deformation and the motion of the blocks is caused by inertial forces, cohesive forces due to bonds, and buoyant force due to water. The material behavior of the individual continuous ice blocks was linear elastic. The simulations were explicit and central difference method was used to advance between the time steps. updating of node positions using Newton's laws for the next time step.

The blocks within the pile were bonded together by freeze bonds (see Figure 1b), which we modelled using initially rigid cohesive elements (Camacho and Ortiz, 1996). A cohesive crack growth process started in a freeze bond, if its stress state was such that

$$\sigma_{cr} \leq \begin{cases} \sqrt{\beta^{-2} t_t^2 + t_n^2} & \text{if } t_n \geq 0 \\ \beta^{-1}(|t_t| - \mu |t_n|) & \text{if } t_n < 0. \end{cases} \tag{1}$$

In this criterion t_t and t_n are the tangential and normal components of the traction vector $\mathbf{t}$ at a bond, respectively, and μ is the friction coefficient. Furthermore, β is the shear stress factor, defined as $\beta = \tau_{cr}/\sigma_{cr}$, where τ_{cr} and σ_{cr} are the shear and tensile strengths of the bond, respectively. Once the failure criterion was reached, the bond went through energy dissipating cohesive crack growth process. During this process, the force between the initially bonded blocks ramped down linearly as the distance between the block points originally belonging to the bond increased as described in detail in Polojärvi and Tuhkuri (2013).

The simulation domain is shown in Figure 2 and the main simulation parameters are given in Table 1. The simulations were performed in two phases: (1) first, a rubble pile with random configuration was generated and then (2) the indentor platen moved down into the rubble. We performed simulations on ridges with four different initial configurations. The freeze bond strength was not constant through the rubble depth but instead decreased linearly to ~ 10 % in the bottom of the rubble (rubble thickness $h \approx 4$ m). A number of freeze bond shear strength values were used in the simulations. As Table 1 shows, the freeze bond shear strength, τ_{cr}, on top of the rubble varied between 5 and 100 kPa. These limits were chosen after values measured for τ_{cr} in earlier experiments. There is no data on freeze bond freeze bond tensile strength, σ_{cr}, values. Here, we used value $\sigma_{cr} = 10$ kPa on top of the rubble in all simulations.

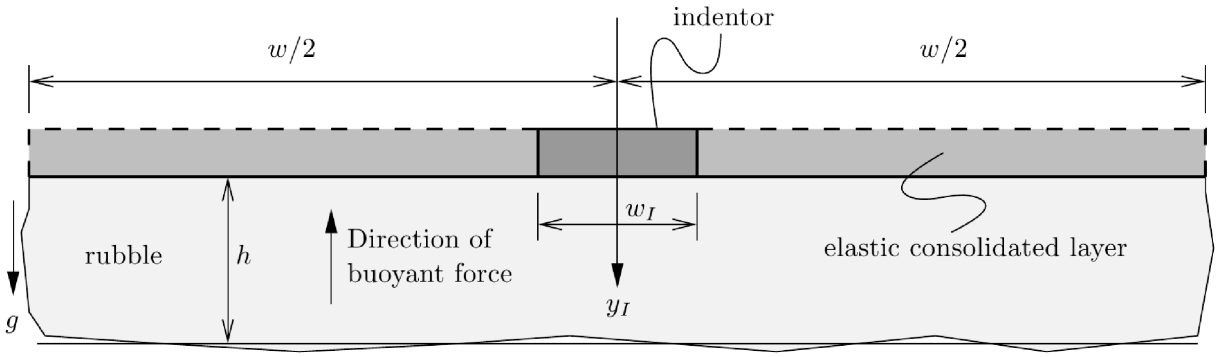

Figure 2: Simulation domain and boundary conditions. The upper boundaries of the consolidated layer (marked with dashed lines) had a rigid boundary condition. The symbols in the figure are as follows: h is the rubble thickness, w the domain width, y_I the direction of indentor penetration, and g the gravitational acceleration. The values of the dimensions in the figure are collected in Table 1.

Table 1: Main parameters used in the simulations. The directions (Dir.) given in the table refer to the global coordinate system in Figure 2. The freeze bond shear and tensile strength values refer to the values on top of the rubble. Indentor size was chosen after Heinonen (2004)

	Parameter	Dir.	Symbol	Unit	Value
General	number of blocks	-	-	-	665
	gravitational acceleration	-	g	ms^{-2}	9.81
	domain width	-	-	m	50
	ndof	-	-	-	~ 150000
Contact	penalty term	-	s	-	$2 \cdot 10^{11}$
	time step	-	Δt	s	$1 \cdot 10^{-6}$
Blocks	length	-	-	m	$0.6 \ldots 1.8$
	thickness	-	-	m	$0.2 \ldots 0.4$
	mass density	-	ρ_b	kgm^{-3}	920
	friction coefficient	-	μ	-	$0.05, 0.3$
	Young's modulus	-	E	GPa	2
	viscous damping constant	-	-	Pas	$2.5 \cdot 10^4$
Water	mass density	-	ρ_w	kgm^{-3}	1010
Rubble	keel depth	-	h	m	~ 4
	bulk porosity	-	η	-	~ 0.25
Indentor	width	x	w_I	m	4
	thickness	y	h_I	m	1
	final velocity	y	v_I	ms^{-1}	0.1
Consolidated layer	thickness	y	-	m	1
	Young's modulus	-	-	GPa	2
Freeze bond	Shear strength	-	τ_{cr}	kPa	$5 \ldots 100$
	Tensile strength	-	σ_{cr}	kPa	10
	Fracture energy	-	G	Jm^{-2}	15

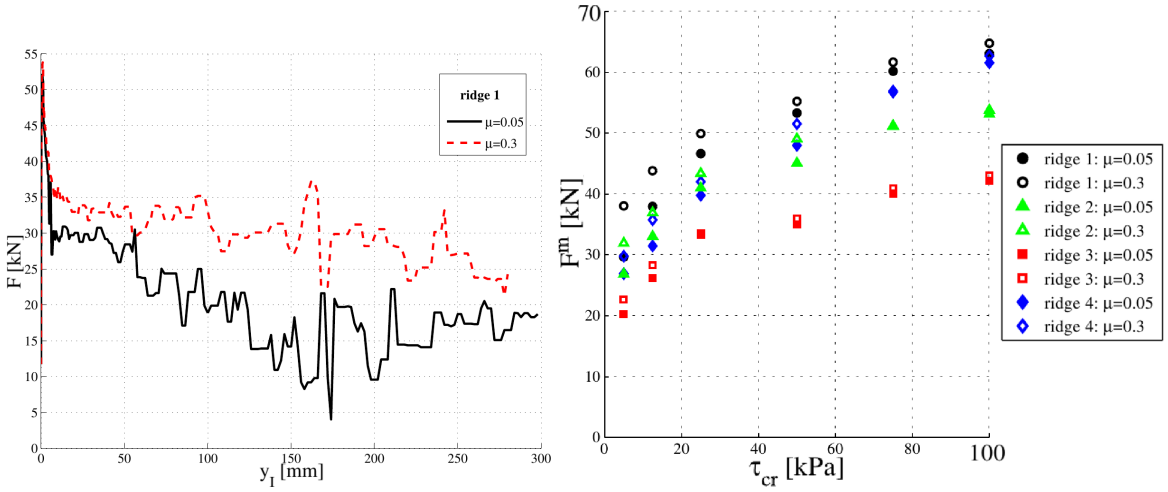

Figure 3: Results from simulations: (a) Typical indentor force-displacement ($F - y_I$) records from the simulations and (b) the maximum load, F^m, as a function of the critical freeze bond shear strength, τ_{cr}. The marker fill color in (b) indicates the F^m values from the simulations with different friction coefficients μ as shown by the legend.

RESULTS AND ANALYSIS

Two typical indentor force-displacement ($F - y_I$) records from the simulations are given in Figure 3a. As the indentor moved down, the indentor force initially increased with high rate and showed a peak value F^m with fairly small indentor displacement. The F^m values depended on the initial configuration of the ridge as Figure 3b shows. As expected, the F^m values increased with the freeze bond shear strength τ_{cr}. Anyhow, the rate $\partial F^m/\partial \tau_{cr}$ of increase was not constant: In general $\partial F^m/\partial \tau_{cr}$ was somewhat higher in the case of weakly bonded ridges. dependency F^m values on the ridge geometry and the the change in the rate $\partial F^m/\partial \tau_{cr}$, were explained by the dependency the rubble failure patterns as described below.

We observed that the effect of bond strength on F^m and on non constant rate $\partial F^m/\partial \tau_{cr}$ were related to differences in the initial failure patterns of the rubble. The initial failure planes directly affect the amount of rubble mass supported by the indentor and thus the load component due to rubble buoyancy. We assessed the effect of the initial rubble failure planes by using the area A_p (defined in Figure 4a) of the plug generated and starting to move down with the indentor in the initial rubble failure.

Figure 4b shows the A_p values as function of τ_{cr} and suggests, that the increase in freeze bond strength induces a change in the initial rubble failure pattern up to a certain τ_{cr} (here up to $\tau_{cr} = 50$ kPa), with no change in the failure patterns with further increase in τ_{cr}. In other words, in the case of weak freeze bonds, the increase in F^m with τ_{cr} is accompanied by a change in the failure patterns. When the bonds are strong, the failure patterns do not change with τ_{cr}.

After the peak, the indentor load decreased up to ~ 150 mm of indentor penetration (see Figure 3a). This post-peak decrease in indentor load was related to the rubble deformation patterns as illustrated in Figure 5a and b. For the following discussion, we should also note, that the area

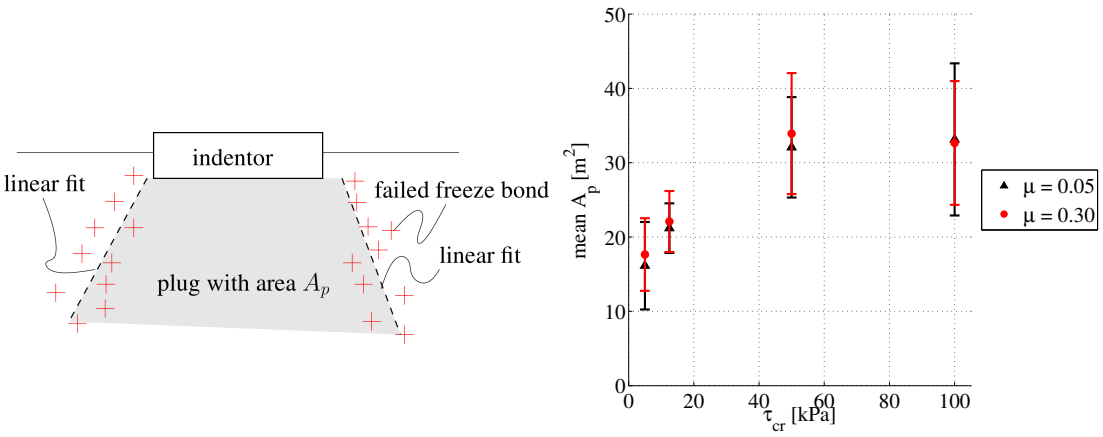

(a) (b)

Figure 4: Effect of the area of the plug A_p forming in the initial failure of the rubble mass: (a) Assessing A_p using the failed freeze bonds within the rubble and (b) the mean values of A_p from all simulations as a function of τ_{cr} with friction coefficient μ values 0.05 and 0.3. The data is from simulations on all ridges with freeze bond tensile strength $\sigma_{cr} = 10$ kPa.

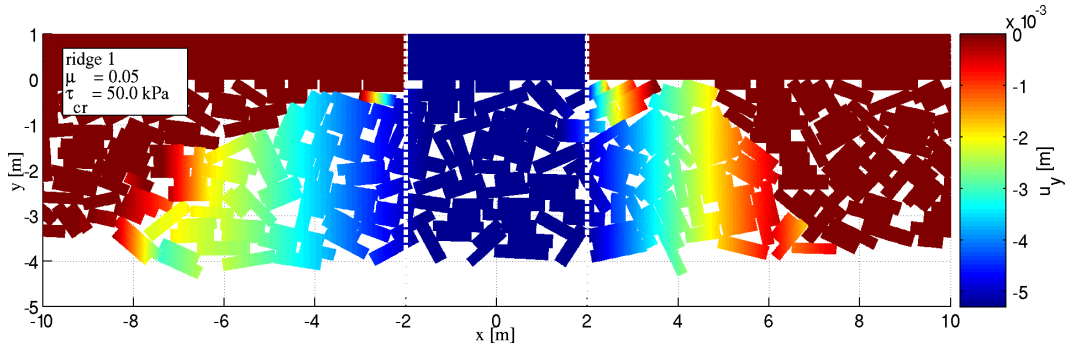

(a)

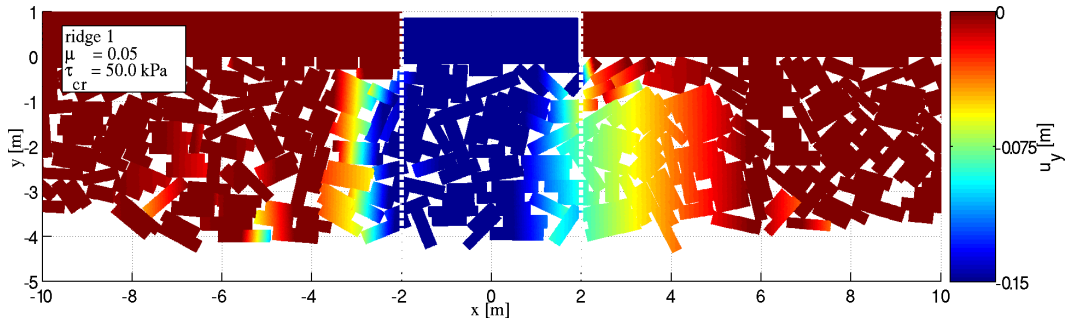

(b)

Figure 5: Displacement field of the rubble and a change in the rubble deformation patterns for a simulated ridge: (a) After initial failure ($y_I = 5$ mm), a large volume of rubble has been cut off the surrounding field, but (b) this volume decreases during further indentor penetration ($y_I = 150$ mm). The colors indicate vertical displacement u_y. Here, $\tau_{cr} = 50$ kPa, $\sigma_{cr} = 10$ kPa, and $\mu = 0.05$.

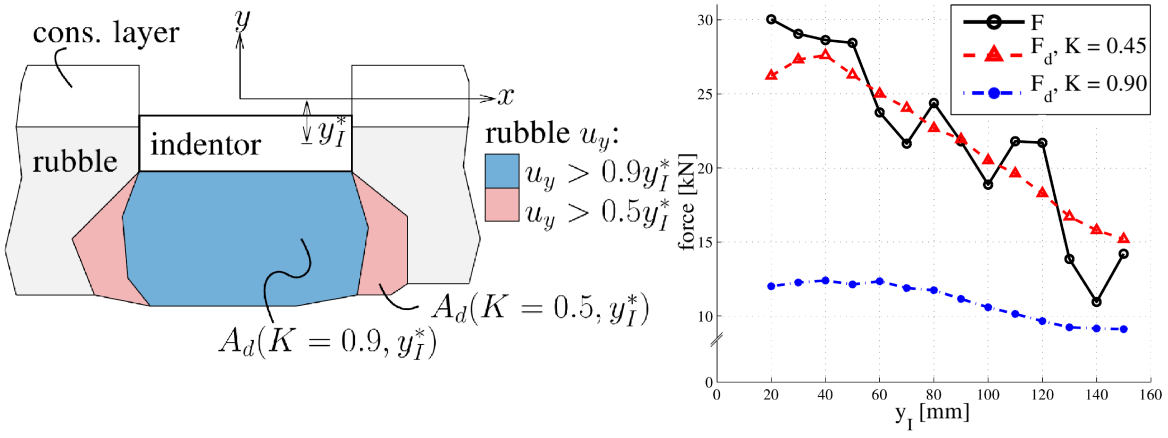

(a) (b)

Figure 6: Post-peak load and deformation patterns: (a) definition of $A_d(K, y_I)$ for $K = 0.5$ and 0.9 – for example the $A_d(K = 0.5, y_I^*)$ at indentor displacement y_I^* includes the rubble with downward displacements of $u_y > 0.5y_I^*$ – and (b) post-peak indentor load F (black line) with the buoyant forces $F_d(K = 0.45, y_I)$ (dashed red line) and $F_d(K = 0.9, y_I)$ (dash dotted blue line) as a function of the indentor displacement y_I mm from the simulation in Figs. 5a and b.

of rubble having the same displacement as the indentor (indicated by darkest blue in the figures) remains approximately equal in the simulation of Figure 5.

We defined the areas of the displaced rubble as illustrated in Figure 6a to study the relation between post-peak load and deformation patterns as follows. At various indentor displacements, y_I, we used downward rubble displacement fields, u_y (such as those in Figures 5a and b) to define areas A_d of the rubble displaced by more than some ratio $K = \{0 \ldots 1\}$ of y_I. For example, the area $A_d(K = 0.5, y_I = 100$ mm$)$ included rubble with $u_y > 0.5 \cdot 100$ mm $= 50$ mm. Then we used areas $A_d(K, y_I)$ to derive a buoyant load

$$F_d(K, y_I) = (1 - \eta)(\rho_w - \rho_i)gA_d(K, y_I), \tag{2}$$

which we compared to the post-peak indentor load with a number of K values. In the previous equation, η is the pile bulk porosity, ρ_w and ρ_i the material densities of water, and ice and g the gravitational acceleration. As an example, the load $F_d(K = 0.5, y_I = 100$ mm$)$ is an estimate for buoyant load of rubble with $u_y \geq 50$ mm.

The three F_d plots in Figure 6b depict the change in the rubble deformation field with indentor displacement. The same change is also seen by comparing Figure 5a and b: The plug which started to move after the initial failure (Figure 5a) dissolved due to bond failures as indentor proceeded its motion, which led to a smaller amount of rubble moving downwards later in the simulation (Figure 5b). Corresponding to this change in rubble deformation field, F and $F_d(K = 0.45, y_I)$ in Figure 6b both decreased with increasing y_I. Furthermore Figure 5a and b show, that the amount of rubble that moved the same amount as the indentor (dark blue area in the figures) remained approximately constant, which explains the smaller decrease in $F_d(K = 0.9, y_I)$ in Figure 6b. the buoyant component and how it changes.

A similar relationship between the deformation fields and the post-peak load levels applied for all simulations. To show this, we derived data sets with values of $A_d(K, y_I)$ with $K =$

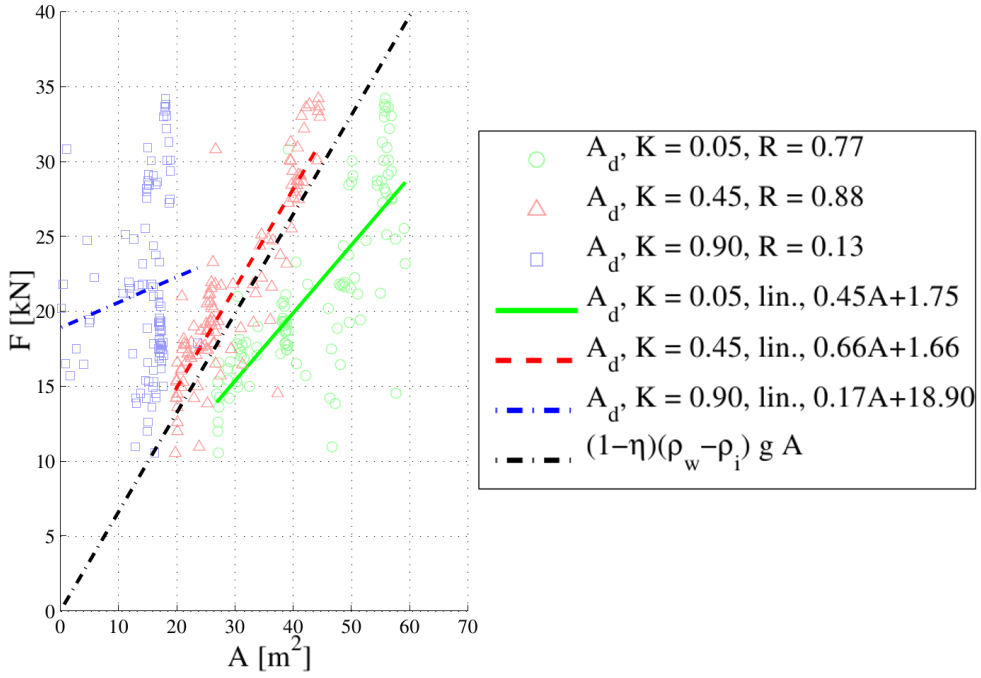

(a)

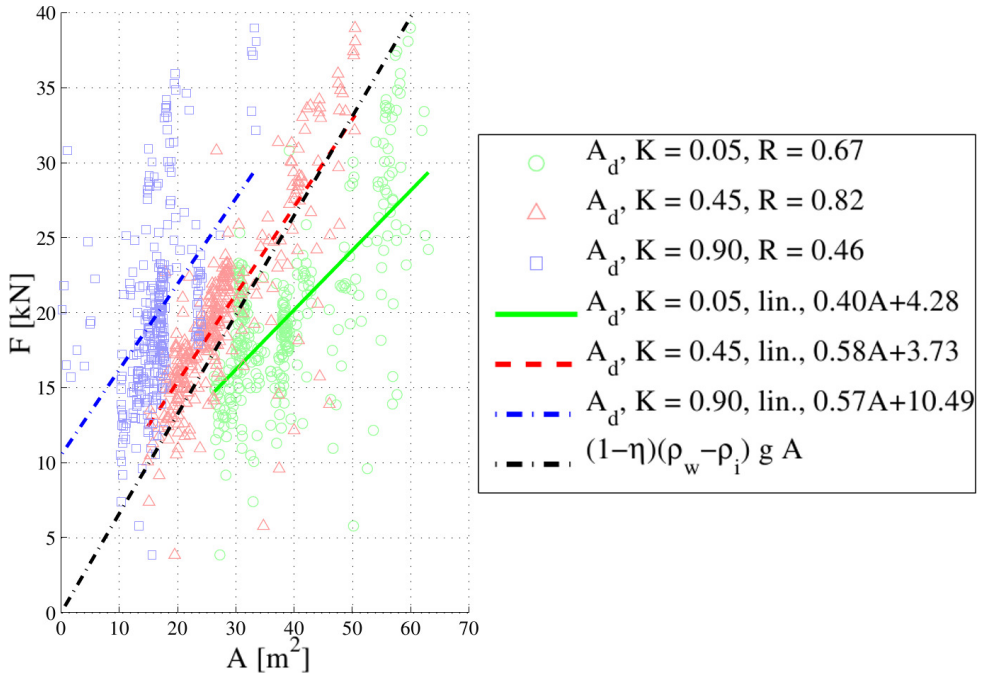

(b)

Figure 7: The data set $F - A_d(K, y_I)$ (see text for details) when $K = \{0.1, 0.5, 0.9\}$ with indentor displacements of $y_I = \{20, 30, 40, \ldots, 150\}$ mm: (a) Simulations on Ridges 1-4 with a freeze bond tensile and shear strength of $\sigma_{cr} = 10$ kPa and $\tau_{cr} = 50$ kPa, respectively, and (b) all simulations. The legend gives the correlation coefficients R and the linear fits of the data sets for each K. Data points from the simulations with both friction coefficients ($\mu = 0.05$ and 0.3) are included in the figure.

$\{0.1, 0.45, 0.9\}$ and $y_I = \{20, 30, 40, \ldots, 150\}$ mm and corresponding F values for each simulation. One such set would include the $F_d(K, y_I)$ and F data given by the markers in Figure 6. The $F - A_d(K, y_I)$ sets from all of the simulations for each $K = \{0.1, 0.45, 0.9\}$ are shown in Figure 7a and b, together with their correlation coefficients (R) and linear fits. Figure 7a gives $F - A_d$ data from the simulations done on all initial configurations with freeze bond shear and tensile strengths of $\tau_{cr} = 50$ kPa and $\sigma_{cr} = 10$ kPa, respectively, and Figure 7b includes the data from all of the simulations. In addition, the figures show a line for buoyant force $F = (1 - \bar{\eta})(\rho_w - \rho_i)gA$, where $\bar{\eta}$ is the mean porosity of the initial configurations.

Figures 6 and 7 illustrate three important findings related to the interpretation of punch through test $F - y_I$ records on the post-peak regime: (1) The assumption, that only the rubble directly under the indentor causes the buoyant load component is incorrect, as (2) the indentor supports a larger volume of displacing rubble, leading to (3) the post-peak load having a large component due to buoyancy, which can decrease and be mistaken for as material softening.

The first two findings in the previous paragraph are shown by the correlation coefficients, R, for the data sets $F - A_d(K, y_I)$ in Figure 7. These are $R = 0.13$ when $K = 0.9$ (no correlation) and $R = 0.88$ when $K = 0.45$ (clear correlation) for the different ridge geometries with constant freeze bond properties (Figure 7a). For all of the simulations, data set $F - A_d(K = 0.9, y_I)$ shown had the value $R = 0.46$, but still data set $F - A_d(K = 0.45, y_I)$ with the value $R = 0.82$ clearly yield the best correlation (Figure 7b). The data set $F - A_d(K = 0.9, y_I)$ show better correlation in Figure 7b than in Figure 7a, which was due to higher $A_d(K = 0.9, y_I)$ values for the highest freeze bond strengths ($\tau_{cr} = 100$ kPa).

In addition to the R values, the lines giving the buoyant load as a function of A in Figure 7a and b support the second finding in both cases, since the data set $F - A_d(K = 0.45, y_I)$ data points in general lie close to the lines in the figures. The last finding is also supported by the data set $F - A_d(K = 0.45, y_I)$ in Figure 7a and b, and was also illustrated by Figure 6: A decrease in $A_d(K = 0.45, y_I)$ leads to a decrease in the post-peak F. Hence, the decrease in F is related to a change in the deformation patterns of the rubble pile, not to the softening of the rubble material itself.

CONCLUSIONS

We modelled ridge keel punch through experiments on partly consolidated ridges. We varied the ridge keel strength by varying the shear strengths of the freeze bonds. We found that the maximum load in the experiments is dependent on initial failure pattern of the rubble, which, on the other hand, is dependent on the strength of the freeze bonds. Similarly, we observed that the post peak-load levels show a clear dependency on the rubble volume being displaced by the indentor platen during the experiment. In the future, a study on the details of the effect of the initial configuration should be carried out together with simulations with more freeze bond tensile to shear strength ratios. Further, a detailed study on the effect of loading rate should be carried out. In the work leading to this paper, only simulations with indentor velocities given in Table 1 and lower were performed, with lower velocities leading to negligible change in the simulation results.

ACKNOWLEGMENTS

The authors wish to acknowledge the support from the Research Council of Norway through the Centre for Research-based Innovation SAMCoT and the support from all SAMCoT partners.

REFERENCES

Camacho, G. and Ortiz, M. (1996). Computational modelling of impact damage in brittle materials. *International Journal of Solids and Structures*, 33(20–22):2899–2938.

Heinonen, J. (2004). *Constitutive modeling of ice rubble in first-year ridge keel*. Doctoral Thesis, TKK. VTT Publications 536. Espoo, Finland, 2004, 142 p, ISSN 1235-0621.

Hopkins, M. (1992). Numerical simulation of systems of multitudinous polygonal blocks. Technical Report 92-22, Cold Regions Research and Engineering Laboratory, CRREL. 69 p.

Liferov, P. and Bonnemaire, B. (2005). Ice rubble behaviour and strength: Part I. review of testing and interpretation of results. *Cold Regions Science and Technology*, 41:135–151.

Liferov, P., Jensen, A., and Høyland, K. (2003). 3D finite element analysis of laboratory punch tests on ice rubble. In *Proceedings of the 17th International Conference on Port and Ocean Engineering under Arctic Conditions, POAC'03*, volume 2, pages 611–621, Trondheim, Norway.

Munjiza, A. (2004). *The combined finite-discrete element method*. John Wiley & Sons Ltd., Chichester, England.

Munjiza, A., Owen, D., and Bićanić, N. (1995). A combined finite-discrete element method in transient dynamics of fracturing solids. 12:145–174.

Paavilainen, J., Tuhkuri, J., and Polojärvi, A. (2009). 2D combined finite–discrete element method to model multi-fracture of beam structures. *Engineering Computations*, 26(6):578–598.

Polojärvi, A. and Tuhkuri, J. (2013). On modeling cohesive ridge keel punch through tests with a combined finite-discrete element method. *Cold Regions Science and Technology*, 85:191–205.

Polojärvi, A., Tuhkuri, J., and Korkalo, O. (2012). Comparison and analysis of experimental and virtual laboratory scale punch through tests. *Cold Regions Science and Technology*, 81:11–25.

Serré, N. (2011). Mechanical properties of model ice ridge keels. *Cold Regions Science and Technology*, 67(3):89–106.